AGU PUBLICATIONS

Radio Science

RESEARCH ARTICLE
10.1002/2014RS005519

Key Points:
- Imaging of the local structure in the electric field using multibeam ISR
- Implements the Lagrange method of undetermined multipliers
- Can be used for imaging the current systems surrounding auroral arcs

Correspondence to:
M. J. Nicolls,
michael.nicolls@sri.com

Citation:
Nicolls, M. J., R. Cosgrove, and H. Bahcivan (2014), Estimating the vector electric field using monostatic, multibeam incoherent scatter radar measurements, *Radio Sci.*, *49*, 1124–1139, doi:10.1002/2014RS005519.

Received 7 MAY 2014
Accepted 21 OCT 2014
Accepted article online 24 OCT 2014
Published online 28 NOV 2014

Estimating the vector electric field using monostatic, multibeam incoherent scatter radar measurements

Michael J. Nicolls[1], Russell Cosgrove[1], and Hasan Bahcivan[1]

[1]Center for Geospace Studies, SRI International, Menlo Park, California, USA

Abstract An algorithm has been developed to image the local structure in the convection electric field using multibeam incoherent scatter radar (ISR) data. The imaged region covers about 4° in magnetic latitude and 8° in magnetic longitude for the specific geometry considered (that of the Poker Flat ISR). The algorithm implements the Lagrange method of undetermined multipliers to regularize the underdetermined problem posed by the radar measurements. The error on the reconstructed image is estimated by mapping the mathematical form to a Bayesian estimate and observing that the Lagrangian method determines an effective a priori covariance matrix from a user-defined regularization metric. There exists a unique solution when the average measurement error is smaller than the average measurement amplitude. The algorithm is tested using synthetic and real data and appears surprisingly robust at estimating the divergence of the field. Future applications include imaging the current systems surrounding auroral arcs in order to distinguish physical mechanisms.

1. Introduction

Advanced Modular Incoherent Scatter Radar systems are monostatic radars capable of beam steering on a pulse-to-pulse basis [*Kelly et al.*, 2009]. With typical interpulse periods in the range 1–10 ms, incoherent integration over tens of seconds or minutes means that measurements from different look directions (or beams) can be considered simultaneous. These systems were developed in order to achieve spatial resolution in the horizontal directions. However, the spatial sampling associated with the monostatic configuration is incomplete and highly irregular so that some sort of algorithm is required to form an image of the physical quantities of interest. In this work, we develop an algorithm for imaging the two-dimensional electric field distribution based on line-of-sight (LOS) velocities measured by a multibeam radar.

Incoherent scatter radars (ISRs) are capable of inferring electron density, electron temperature, ion temperature, and LOS velocity from the backscattered signal. (Additional parameters can sometimes be inferred as well.) This is typically accomplished by fitting a theoretical autocorrelation function through a finite number of complex "lag products" formed from the backscatter, which constitute measurements (weighted by some ambiguity function) of points on the autocorrelation function [*Dougherty and Farley*, 1960]. Imaging the scalar parameters (density and temperature) amounts to a resampling of the measurements in space, with nontrivial interpolation, so that results can be inferred from the imaged products. Previous efforts in this regard include *Nicolls et al.* [2007], who imaged polar mesosphere summer echoes, *Semeter et al.* [2009] who imaged auroral forms, *Nygren et al.* [2011] who used stochastic inversion, and *Dahlgren et al.* [2012] who imaged polar cap structures.

In this work, we consider the more difficult problem of imaging vector quantities, in particular the electric field. Imaging the vector electric field is more difficult because the radar does not measure the full electric field vector, even at a single point. Rather, the radar measures the LOS velocity, which provides only the component of the electric field in the direction perpendicular to the beam (and to the geomagnetic field, $\mathbf{B}_0$). Information on the other component exists only in measurements from other beams, which are not in the same location. Hence, inferences with respect to the vector electric field can only be made by way of some assumption with respect to the way that the electric field varies in space. For example, *Butler et al.* [2010] and *Semeter et al.* [2010] assumed that the electric field did not vary in certain predefined regions of size large enough so that two components of the electric field could be inferred from the collection of LOS velocity measurements in the regions. Their results for the electric field around an auroral arc are very intriguing and provide motivation for our effort.

The approach we take is based in the concept of regularization [e.g., *Neumaier*, 1998]. The radar measurements contain information about the vector electric field, but they do not completely specify it at any location. There is a multidimensional solution space of possible electric field distributions consistent with the measurements, and it is necessary to introduce some additional assumption or information that identifies a single solution from within the solution space. We attack this general regularization problem by framing it as a problem in constrained minimization, which can be solved using the method of Lagrange multipliers [e.g., *Goldstein*, 1980; *Boyd and Vandenberghe*, 2009]. The constraint that we impose is that the reconstructed electric field reproduces the LOS velocity measurements with allowance for the measurement error. Among the electric fields that satisfy this constraint, we identify the unique one that minimizes a measure of curvature and absolute gradient. The definition of this measure constitutes the additional assumption necessary to determine a unique solution.

In section 2.1, measurement of the LOS velocities is discussed and notation is defined for relating the LOS velocity to the components of the vector-valued flow velocity parallel and perpendicular to the geomagnetic field ($\mathbf{B}_0$). In section 2.2, a linear forward model is defined appropriate for regularized solution. In section 2.3, a uniform background flow solution is defined, which contains our estimate for the parallel to $\mathbf{B}_0$ component. In section 2.4, the method of Lagrange multipliers is formulated and solved in terms of a regularizing measure defined as a general 2-norm. In section 2.5, our specific choice for the regularizing measure is defined, and the condition for existence and uniqueness of the vector electric field solution is formulated. In section 3.1, the performance of the algorithm is investigated using synthetic data. In section 3.2, the performance of the algorithm is investigated using data from the Poker Flat Incoherent Scatter Radar (PFISR).

2. Estimating the Vector Electric Field

2.1. Line-of-Sight Velocity Components

There are several "classical" ways of estimating LOS velocity from the incoherent scatter spectrum. Fundamentally, the LOS velocity corresponds to the Doppler shift of the spectrum, and a spectral moment method or a fit to the phase angle can both be used [e.g., *Skolnik*, 1980]. However, for asymmetric (noisy) spectra these methods may introduce biases. In our general analysis, we estimate the LOS component of the velocity from a fit to the full incoherent scatter autocorrelation function (including both the real and imaginary parts). Errors on the fit are evaluated by estimating the Jacobian at the output parameter value.

We will assume that the electric field maps along $\mathbf{B}_0$ without attenuation. Hence, the LOS velocity measurements and our results for electric field can be understood as applying to whole magnetic field lines. However, the LOS velocity measurements are subject to range ambiguity that depends on the type of pulse coding. Roughly speaking, this means that the measured velocity is actually an average over some "resolution" distance along the LOS, which corresponds to a resolution in the direction transverse to $\mathbf{B}_0$ that depends on the LOS angle with $\mathbf{B}_0$. If a simple, uncoded long pulse is used, the resolution could be poor enough to warrant compensation by altering the way data are mapped to the grid in what follows. The data could be spread over regions that reflect the varying transverse resolution. However, we have elected not to introduce this complexity and instead consider each LOS measurement as applying to the center of its ambiguity range.

Consider the local vector ion velocity written in terms of the perpendicular eastward, perpendicular northward, and antiparallel components with respect to $\mathbf{B}_0$,

$$\mathbf{v} = [v_{\perp \mathrm{e}}\ v_{\perp \mathrm{n}}\ v_{\parallel}], \tag{1}$$

and for convenience define notation for its decomposition into perpendicular and parallel vectors:

$$\mathbf{v}_{\perp} = [v_{\perp \mathrm{e}}\ v_{\perp \mathrm{n}}\ 0], \quad \mathbf{v}_{\parallel} = [0\ 0\ v_{\parallel}]. \tag{2}$$

Similarly, define $\mathbf{A}_i$, the unit vector in the direction of the ith beam, along with its decomposition into parallel and perpendicular vectors:

$$\begin{aligned} \mathbf{A}_i &= \mathbf{A}_{\perp i} + \mathbf{A}_{\parallel i} \\ \mathbf{A}_{\perp i} &= [A_{\perp \mathrm{e},i}\ A_{\perp \mathrm{n},i}\ 0] \\ \mathbf{A}_{\parallel i} &= [0\ 0\ A_{\parallel}]. \end{aligned} \tag{3}$$

We will sometimes refer to $\mathbf{A}_i$ as the ith measurement vector. Following *Heinselman and Nicolls* [2008], an LOS component velocity measurement $\tilde{v}_{\text{los},i}$, which is the LOS component velocity $v_{\text{los},i}$ measured with error e_i, can be written as

$$\tilde{v}_{\text{los},i} = v_{\text{los},i} + e_i = \mathbf{A}_i\mathbf{v}_i + e_i = \mathbf{A}_{\perp i}\mathbf{v}_{\perp i}^{\dagger} + \mathbf{A}_{\parallel i}\mathbf{v}_{\parallel i}^{\dagger} + e_i, \tag{4}$$

where we use matrix notation for the inner product by considering spatial vectors to be 1×3 matrices, with superscript † indicating the transpose operation (i.e., $\mathbf{a} \cdot \mathbf{b} = \mathbf{a}\mathbf{b}^{\dagger}$). This matrix notation will be exploited below to fold vector operations into matrix equations. The subscript i on $\mathbf{v}_i$, $\mathbf{v}_{\perp i}$, and $\mathbf{v}_{\parallel i}$ indicates that these are the velocities at the location of the ith measurement. Throughout this paper the superscript $\tilde{}$ refers to a measured quantity and the superscript $\hat{}$ refers to an estimated quantity.

2.2. Forward Model

Our goal is to estimate a two-dimensional electric field vector perpendicular to the geomagnetic field, i.e., $\mathbf{E}(x, y)$ where x and y are the two spatial coordinates. In doing so, we will also estimate the parallel component of the flow velocity, $\mathbf{v}_{\parallel}$, but will assume that this quantity is spatially uniform. This latter criterion is a necessary one given the practical limitations of a monostatic radar and the expected relatively small contribution from the parallel motion. However, for certain types of ion upflow events the parallel velocity might have sufficient local enhancements to warrant reconsidering this decision, although this would introduce significant additional complexity. For the present work we begin the process of estimating a two-dimensional flow field by decomposing the problem into a background uniform flow field (which will contain the parallel component) and a spatially varying perturbation field.

The forward model with spatial dependencies explicitly defined can thus be written as

$$\mathbf{v}(x, y) = \mathbf{v}_0 + \frac{\delta\mathbf{E}(x, y) \times \mathbf{B}}{|B|^2} \tag{5}$$

where $\mathbf{v}_0 = \mathbf{v}_{\perp 0} + \mathbf{v}_{\parallel 0}$ is some uniform "background" flow. In writing this equation, we assume that the vector ion drift is related to the electric field through the relation,

$$\mathbf{v}_{\perp}(x, y) = \frac{\mathbf{E}(x, y) \times \mathbf{B}}{|B|^2} = \mathbf{v}_{\perp 0} + \frac{\delta\mathbf{E}(x, y) \times \mathbf{B}}{|B|^2}, \tag{6}$$

which gives rise to the term "convection electric field."

In developing our approach, we considered including a constant electric field gradient in $\mathbf{v}_0$, out of concern that the regularization methods defined below may not be optimal for reproducing gradients. Although our method does not specify a fixed boundary, it will perform best when the actual boundary is relatively uniform. However, it turns out that estimation of a constant gradient solution is poorly conditioned, at least for the monostatic radar configuration. Estimating a gradient amounts to estimating a wavelength much longer than sampling region, which is difficult due to the usual Fourier limitations.

The next step is to write the perpendicular, spatially varying electric field as the gradient of a potential function, $\phi(x, y)$,

$$\delta\mathbf{E}(x, y) = -\nabla\phi(x, y), \tag{7}$$

where $\phi(x, y)$ is the electric potential. In writing this equation, we are assuming that the electric field is electrostatic. This approach amounts to assuming that the divergence of the $\mathbf{E} \times \mathbf{B}$ flow field, $\nabla \cdot \mathbf{v}_{\perp}$, is zero or that the F region ionosphere is incompressible.

With a measurement $\tilde{v}_{\text{los},i}$ defined as in equation (4), we can write the forward model as

$$\tilde{v}_{\text{los},i} = \mathbf{A}_i\mathbf{v}_0^{\dagger} - \mathbf{T}_i\nabla^{\dagger}\phi(x_i, y_i) + e_i, \tag{8}$$

where $\mathbf{T}_i = (\mathbf{B} \times \mathbf{A}_i)/|B|^2$. The last term can be understood through the vector identity

$$-\mathbf{T}_i\nabla^{\dagger}\phi(x_i, y_i) = \mathbf{T}_i \cdot \delta\mathbf{E}(x_i, y_i) = (\mathbf{B} \times \mathbf{A}_i) \cdot \delta\mathbf{E}(x_i, y_i)/|B|^2 = \mathbf{A}_i \cdot (\delta\mathbf{E}(x_i, y_i) \times \mathbf{B})/|B|^2,$$

and referring to equations (4) and (5). We assume that the covariance matrix of the measurements, $\mathbf{C}$, is also known. This matrix is typically assumed to be diagonal with variance σ_i^2, where σ_i is the standard deviation of the measurements derived through the spectral fitting process, as mentioned in section 2.1.

2.3. Uniform Velocity Estimate

By writing the forward model as the sum of a constant-flow solution and the gradient of a potential function, as in equation (5), we are able to treat the problem in two steps. We first estimate a solution to the measurements assuming a constant-flow field and then solve for the remaining spatially varying field. With a set of N measurements, we can define matrices

$$\tilde{\mathbf{v}}_{\text{los}} = \begin{bmatrix} \tilde{\mathbf{v}}_{\text{los},1} \\ \tilde{\mathbf{v}}_{\text{los},2} \\ \vdots \\ \tilde{\mathbf{v}}_{\text{los},N} \end{bmatrix}, \quad \mathbf{e} = \begin{bmatrix} e_1 \\ e_2 \\ \vdots \\ e_N \end{bmatrix}. \tag{9}$$

The linear model for the uniform flow solution can then be written as

$$\tilde{\mathbf{v}}_{\text{los}} = \mathbf{A}\mathbf{v}^{\dagger} + \mathbf{e}, \tag{10}$$

where measurement matrix $\mathbf{A}$ is size $N \times 3$ with rows corresponding to $\mathbf{A}_i$. We define $\mathbf{v}_0$ as

$$\hat{\mathbf{v}}_0 = \left(\mathbf{A}^{\dagger}\mathbf{C}^{-1}\mathbf{A}\right)^{-1}\mathbf{A}^{\dagger}\mathbf{C}^{-1}\tilde{\mathbf{v}}_{\text{los}}, \tag{11}$$

which is the maximum likelihood estimate for $\mathbf{v}$ given the assumption of a uniform flow field obeying the linear model. The parallel component has been retained so that $\hat{\mathbf{v}}_0$ contains our estimate for the parallel ion velocity.

We use the prime superscript to denote the LOS velocities with the constant-flow portion removed, i.e.,

$$\tilde{\mathbf{v}}'_{\text{los}} = \tilde{\mathbf{v}}_{\text{los}} - \mathbf{A}\hat{\mathbf{v}}_0^{\dagger}, \tag{12}$$

which we assume to be consistent with flow that is purely transverse to $\mathbf{B}_0$.

2.4. Electric Potential Solution

We would now like to estimate the spatially varying part of the electric field associated with the $\delta\mathbf{E} \times \mathbf{B}_0$ flow, $\mathbf{v}_{\perp} - \mathbf{v}_{\perp 0}$. We frame the problem as estimation of a potential function on the points of a fine grid, which overlays the measured LOS velocities. From equations (8) and (12), the linear problem can be written as

$$\tilde{\mathbf{v}}'_{\text{los}} = \mathbf{M}\boldsymbol{\Phi} + \mathbf{e} \tag{13}$$

where $\tilde{\mathbf{v}}'_{\text{los}}$ is the $N \times 1$ vector of measurements with errors $\mathbf{e}$ ($N \times 1$) and $\boldsymbol{\Phi}$ is a vector of size $M \times 1$ containing the electric potential (ϕ) at each point on the grid. Consider a two-dimensional grid of size $M_x \times M_y$ and then reorder the points such that $\boldsymbol{\Phi}$ is an $M = (M_x M_y) \times 1$ column vector. The $N \times M$ "measurement matrix" $\mathbf{M}$ realizes the operation $-\mathbf{T}_i\nabla^{\dagger}$ from equation (8) for all the LOS velocity measurements, with results distributed along a column vector. Practically, $\mathbf{M}$ is formed from matrices that realize second-order accuracy, central finite difference approximations for the derivatives in both dimensions ($\boldsymbol{\nabla}_x$ and $\boldsymbol{\nabla}_y$, both size $M \times M$), and multiplying these by $N \times M$ matrices ($\mathbf{T}_x$ and $\mathbf{T}_y$) that perform the appropriate projections of the electric field at the appropriate grid points; i.e.,

$$\mathbf{M} = -\mathbf{T}_x\boldsymbol{\nabla}_x - \mathbf{T}_y\boldsymbol{\nabla}_y. \tag{14}$$

For N measurements ($i = 1, 2, \ldots, N$) and a solution grid with $M > N$ points, equation (13) poses an underdetermined linear problem with an $M - N$ dimensional solution space for $\boldsymbol{\Phi}$. We need to choose a solution from this solution space based on some reasonable criteria. To do this, we follow the Lagrangian method described by *Cosgrove et al.* [2013], which was motivated by the maximum entropy method described by *Hysell and Chau* [2006]. We seek the unique solution that extremizes the norm $\|\boldsymbol{\Phi}\|^2_{\mathbf{G}}$ (i.e., $\boldsymbol{\Phi}^{\dagger}\mathbf{G}\boldsymbol{\Phi}$) for some matrix $\mathbf{G}$ subject to the constraint imposed by equation (13) in addition to the constraint

$$\|\mathbf{e}\|^2_{\mathbf{C}^{-1}} = N - 1, \tag{15}$$

where, as already mentioned, $\mathbf{C}$ is the covariance matrix for the LOS measurements. The left-hand side of (15) is known as the χ^2 parameter, which is a measure of the error in comparison to the expected error. For a Gaussian probability distribution, $N-1$ is the most likely value for χ^2. Therefore, we can state our "reasonable criteria" in words as follows: Among the set of solutions that achieve the most probable tightness of fit to

the data, we choose the one that minimizes the norm $\|\mathbf{\Phi}\|_{\mathbf{G}}^2$. An alternative approach to constraining the "total error" would be to constrain the maximum allowable deviation from individual data points. However, this approach would be more sensitive to outliers which might be a significant problem.

Finding the solution just described is a problem in constrained minimization, which can be solved using the method of Lagrange multipliers [*Goldstein*, 1980; *Boyd and Vandenberghe*, 2009]. The Lagrangian for the problem is

$$\mathcal{L} = \|\mathbf{\Phi}\|_{\mathbf{G}}^2 + \lambda^\dagger \left(\tilde{\mathbf{v}}'_{\text{los}} - \mathbf{e} - \mathbf{M}\mathbf{\Phi}\right) + \Omega\left(\|\mathbf{e}\|_{\mathbf{C}^{-1}}^2 - N + 1\right), \tag{16}$$

where λ is an $N \times 1$ vector of Lagrange multipliers and Ω is an additional Lagrange multiplier for the constraint given by equation (15). The solution $\mathbf{\Phi}$ to the constrained extremization problem is found by minimizing the Lagrangian with respect to $\mathbf{\Phi}$, $\mathbf{e}$, and the Langrange multipliers (simultaneously). It can be found by forming the partial derivatives with respect to these quantities, setting them equal to zero, and solving the resulting equations. Undertaking this results in the equations

$$\hat{\mathbf{\Phi}} = \left(\mathbf{M}^\dagger \mathbf{C}^{-1} \mathbf{M} + \alpha \mathbf{G}\right)^{-1} \mathbf{M}^\dagger \mathbf{C}^{-1} \tilde{\mathbf{v}}'_{\text{los}} \tag{17}$$

$$0 = \tilde{\mathbf{v}}'^{\dagger}_{\text{los}} \left(\mathbf{C} + \frac{1}{\alpha}\mathbf{M}\mathbf{G}^{-1}\mathbf{M}^\dagger\right)^{-1^\dagger} \mathbf{C} \left(\mathbf{C} + \frac{1}{\alpha}\mathbf{M}\mathbf{G}^{-1}\mathbf{M}^\dagger\right)^{-1} \tilde{\mathbf{v}}'_{\text{los}} - N + 1. \tag{18}$$

Equation (18) can be solved for alpha using a one-dimensional search algorithm. Once two values have been identified that make the right-hand side positive and negative, respectively, the next trial value is chosen half way in between, etc. With α determined in this way, the estimate $\hat{\mathbf{\Phi}}$ is found by performing the matrix multiplication in equation (17). Note that equation (17) has the form of Tikhonov regularization with parameter $\sqrt{\alpha}$. Hence, the Lagrangian method has provided a natural way to choose the regularization parameter.

Interpreting equation (17) as a Bayesian estimate, we see that the term $\alpha\mathbf{G}$ plays the role of the inverse of the covariance matrix for the a priori probability distribution. Therefore, defining Σ_e by $\Sigma_e^{-1} = \alpha\mathbf{G}$, the a posteriori covariance matrix for the equivalent Bayesian estimate becomes

$$\hat{\Sigma}_{\mathbf{\Phi}} = \left(\mathbf{M}^\dagger \mathbf{C}^{-1} \mathbf{M} + \Sigma_e^{-1}\right)^{-1}. \tag{19}$$

This interpretation allows us to estimate the errors on the electric potential. The electric field covariance matrix can also be readily computed using standard matrix transformations, e.g.,

$$\hat{E}_x = -\nabla_x \hat{\mathbf{\Phi}},\ \hat{\Sigma}_{E_x} = \nabla_x \hat{\Sigma}_{\mathbf{\Phi}} \nabla_x^\dagger. \tag{20}$$

2.5. Regularization Matrix and Condition for a Unique Solution

As described above, among the solutions that achieve the most probable tightness of fit to the data, we choose the one that minimizes the norm $\|\mathbf{\Phi}\|_{\mathbf{G}}^2 = \mathbf{\Phi}^\dagger \mathbf{G} \mathbf{\Phi}$. Here we choose what quantity we want the norm to evaluate. An illustrative choice for $\mathbf{G}$ is $\mathbf{G} = \mathbf{\Gamma}^\dagger \mathbf{\Gamma}$, where $\mathbf{\Gamma\Phi}$ is a quantity that we intuitively feel should be as small as possible in the mean squared sense. For example, if $\mathbf{\Gamma}$ acting on $\mathbf{\Phi}$ produces the curvature of the surface that Φ defines over the grid, then our solution would minimize the mean squared curvature. In this case our solution for $\mathbf{\Phi}$ would be the smoothest possible, in a very real sense. However, more elaborate choices for $\mathbf{\Gamma}$ allow for tailoring of the solution in specific ways.

We consider a $\mathbf{G}$ composed of three components, one with norm equal to the sum of the squared electric field magnitudes ($\mathbf{G}_0$), the second with norm equal to the sum of the squared electric field absolute component gradients ($\mathbf{G}_1$), and the third with norm equal the sum of the squared electric field component Laplacians ($\mathbf{G}_2$):

$$\mathbf{G} = a\mathbf{G}_0 + b\mathbf{G}_1 + c\mathbf{G}_2. \tag{21}$$

Specifically,

$$\|\mathbf{\Phi}\|^2_{\mathbf{G}_0} = \sum_{i=1}^{M} (E_{xi})^2 + (E_{yi})^2,$$
$$\|\mathbf{\Phi}\|^2_{\mathbf{G}_1} \Rightarrow \sum_{i=1}^{M} \left(\frac{\partial E_{xi}}{\partial x}\right)^2 + \left(\frac{\partial E_{xi}}{\partial y}\right)^2 + \left(\frac{\partial E_{yi}}{\partial x}\right)^2 + \left(\frac{\partial E_{yi}}{\partial y}\right)^2$$
$$\|\mathbf{\Phi}\|^2_{\mathbf{G}_2} \Rightarrow \sum_{i=1}^{M} \left(\frac{\partial^2 E_{xi}}{\partial x^2}\right)^2 + \left(\frac{\partial^2 E_{xi}}{\partial y^2}\right)^2 + \left(\frac{\partial^2 E_{yi}}{\partial x^2}\right)^2 + \left(\frac{\partial^2 E_{yi}}{\partial y^2}\right)^2, \quad (22)$$

where the double arrow replaces the equals sign in cases where derivatives are to be approximated by finite differences. Hence, we have

$$\mathbf{\Phi}^\dagger \mathbf{G} \mathbf{\Phi} = a\|\mathbf{\Phi}\|^2_{\mathbf{G}_0} + b\|\mathbf{\Phi}\|^2_{\mathbf{G}_1} + c\|\mathbf{\Phi}\|^2_{\mathbf{G}_2},$$

and we can choose the weights as a function of position on the grid to determine what manner of regularization we wish to impose in that area. In practice, we have chosen $a = b = 0,\ c = 1$ in the central area of the grid where there is good support from the LOS measurements. However, outside of this area we have chosen $a = c = 0,\ b = 1$. This gives a "minimum total curvature" interpolation of the electric field between beams but forces the electric field to approach a single constant value far from the measurement region, which eliminates the need to fix boundary conditions.

Each component of $\mathbf{G}$ is composed of a sum of matrices that implement the appropriate operator in the appropriate direction and on the appropriate component. For example,

$$\mathbf{G}_2 = \mathbf{\Gamma}^\dagger_{mm}\mathbf{\Gamma}_{mm} + \mathbf{\Gamma}^\dagger_{nn}\mathbf{\Gamma}_{nn} + \mathbf{\Gamma}^\dagger_{nm}\mathbf{\Gamma}_{nm} + \mathbf{\Gamma}^\dagger_{mn}\mathbf{\Gamma}_{mn} \quad (23)$$

where, for example, $\mathbf{\Gamma}_{nm}\mathbf{\Phi}$ is a vector containing the finite difference approximations for $\left(\frac{\partial^2 E_{xi}}{\partial y^2}\right)$, for all i.

The form given for $\mathbf{G}$ in equation (23) ensures that $\mathbf{G}$ is positive definite. This allows us to show that the right-hand side of equation (18) is monotonic in α. As $\alpha \to 0$ the right-hand side of equation (18) approaches $1 - N$, which is negative for $N > 1$. Therefore, there will be a unique solution to equation (18) if and only if the right-hand side approaches a positive number as $\alpha \to \infty$. Letting $\alpha \to \infty$, we obtain the condition

$$\tilde{\mathbf{v}}'^\dagger_{\text{los}}\mathbf{C}^{-1}\tilde{\mathbf{v}}'_{\text{los}} - N + 1 > 0. \quad (24)$$

Therefore, there will be a unique electric field solution associated with the LOS measurements $\tilde{\mathbf{v}}'_{\text{los}}$ with error covariance matrix $\mathbf{C}$ if and only if the condition in equation (24) is satisfied. The condition is not satisfied when the errors become too large. On average, the errors on the LOS velocities need to be smaller than the absolute LOS velocities. For example, in the case of a minimum curvature criteria ($\mathbf{G} = \mathbf{G}_2$), excessively large errors allow the χ^2 constraint to be achieved by a plane (zero curvature), after which further increase in the errors provides for a family of planes that achieve the χ^2 constraint. In practice, we have found that the solution occasionally becomes nonunique. However, this is very rare and simply indicates the condition that the measurements are not of sufficient quality to find a unique solution.

3. Example Results

3.1. Examples With Synthetic Data

While we have demonstrated uniqueness of the proposed methodology, we must show that the assumptions are valid and able to reproduce expected two-dimensional electric field structures. In order to assess the performance of the algorithm, we have generated synthetic electric potential patterns for a number of scenarios, sampled the associated LOS velocities with various radar beam configurations, added representative noise to the measurements, and inverted the measurements using the methodology described. In addition, we have explored a number of options for $\mathbf{G}$ using this simulation approach before converging on the total curvature approach described in section 2.5. Here we present the results for three potential pattern configurations: a zonally extended blob (i.e., extended normal with respect to the radar boresight), a meridionally extended blob (i.e., extended parallel to the radar boresight), and a more complicated example with two localized potential blobs, sampled with realistic measurement errors. These errors were based on a polynomial fit to PFISR measurements and increase as range squared.

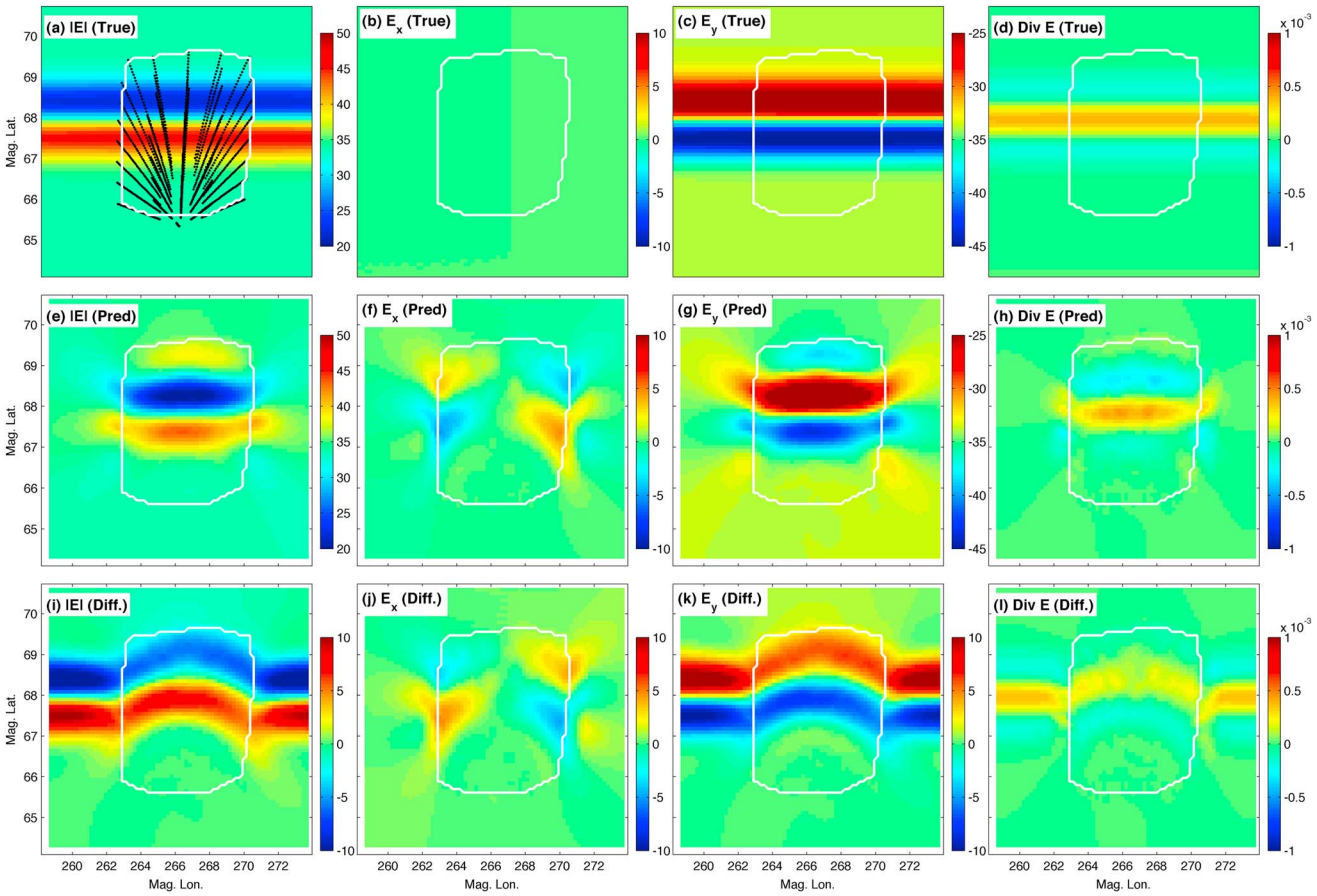

Figure 1. (a–d) Magnitude, zonal component, meridional component, and divergence of the electric field for a zonally extended potential blob. (e–h) Estimated fields using the methodology described in the text. (i–l) Difference between the true and estimated fields. In Figure 1a, the black dots correspond to where the line-of-sight velocity was sampled. In all panels, the white border delineates a mask used for **G**; see text for details. Note that the color bars for the difference panels are not the same as the ones for the actual and estimated full amplitudes.

Figure 1 shows the magnitude of the electric field (a), the zonal electric field (b), the meridional electric field (c), and the divergence of the electric field (d) for the zonally extended potential blob, which also includes a background meridional field. This case satisfies the zonal invariance assumption usually made for ISRs in the auroral region so that, for example, the method of *Heinselman and Nicolls* [2008] would work well (except that having made the assumption, there would be no way to know it was satisfied). Here $\hat{x}$ is zonal (positive eastward) and $\hat{y}$ is meridional (positive northward). Reconstructed images are shown in Figures 1e–1h for the same fields. In this case, we have sampled the true fields with measurement errors significantly smaller (~10 times) than the expected radar errors in order to demonstrate features of the algorithm. Line-of-sight velocities were sampled at the black points shown in Figure 1a, which are derived from a true 41-beam "imaging mode" used at PFISR (results of which are presented in section 3.2). The white border in all panels represents the delineation of the measurement region inside of which there is good support from the LOS velocity measurements and where we use a total curvature minimization (see section 2.5). Outside of this region, a total gradient regularization is imposed that will force the solution to approach a constant value. Finally, the differences between the true and reconstructed images are shown in Figures 1i–1l.

We can observe several features in the reconstructions:

1. The algorithm is able to reproduce the constant background meridional field, and the main features of the zonally extended potential blob, mainly a negative to positive deviation in the meridional electric field with increasing latitude, within the region supported by the measurements.
2. Outside of that region, the fields go to a constant value of electric field. This is the expected behavior since in this region our choice of **G** (see section 2.5) will minimize the first derivative of the field and tend toward a constant value in the absence of data.

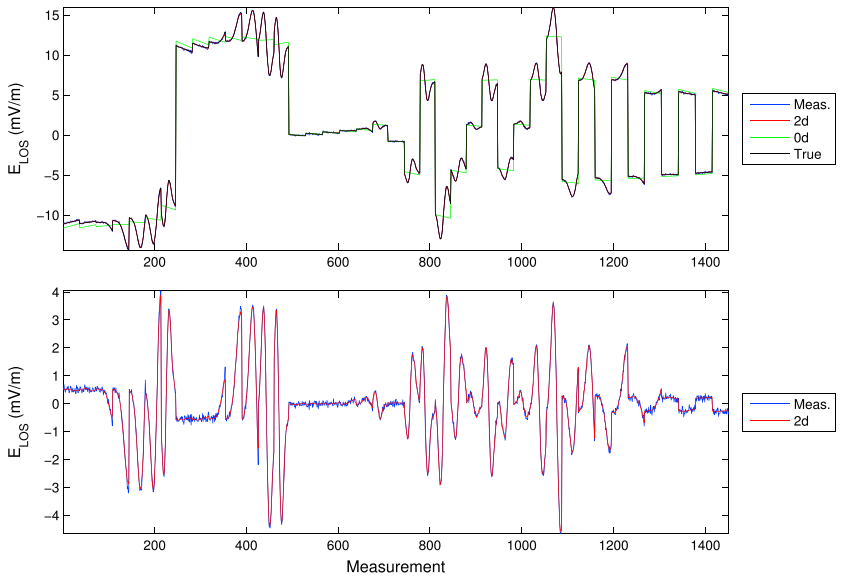

Figure 2. For the case of Figure 1. (top) Line-of-sight electric fields, concatenated for all beams: true values (black), measured values (blue), background field solution (green), and two-dimensional solution (red). (bottom) Measured line-of-sight electric fields with estimated background field subtracted (blue) along with the forward model fits from the two-dimensional solution (red).

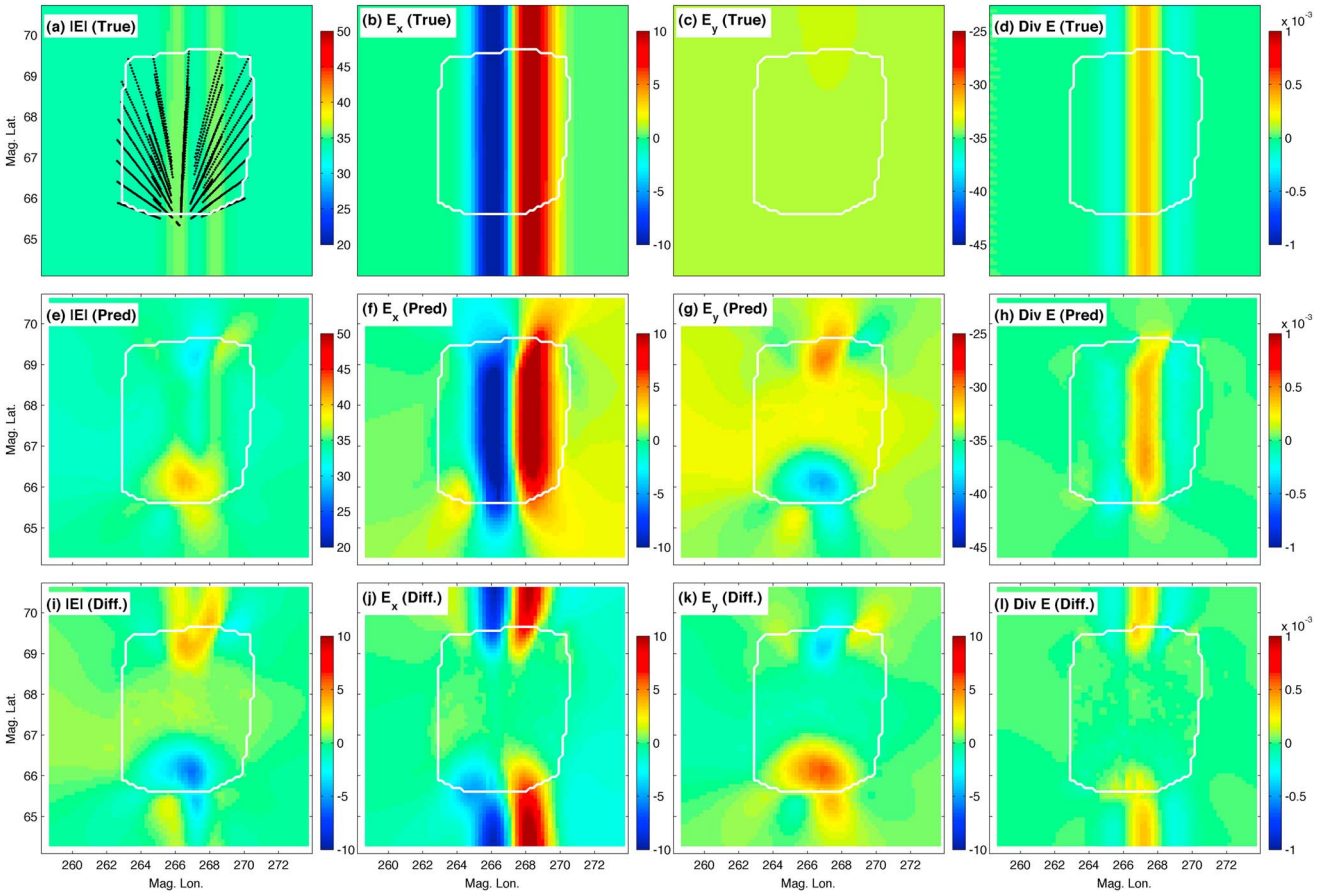

Figure 3. Same as Figure 1 for a meridionally extended potential blob.

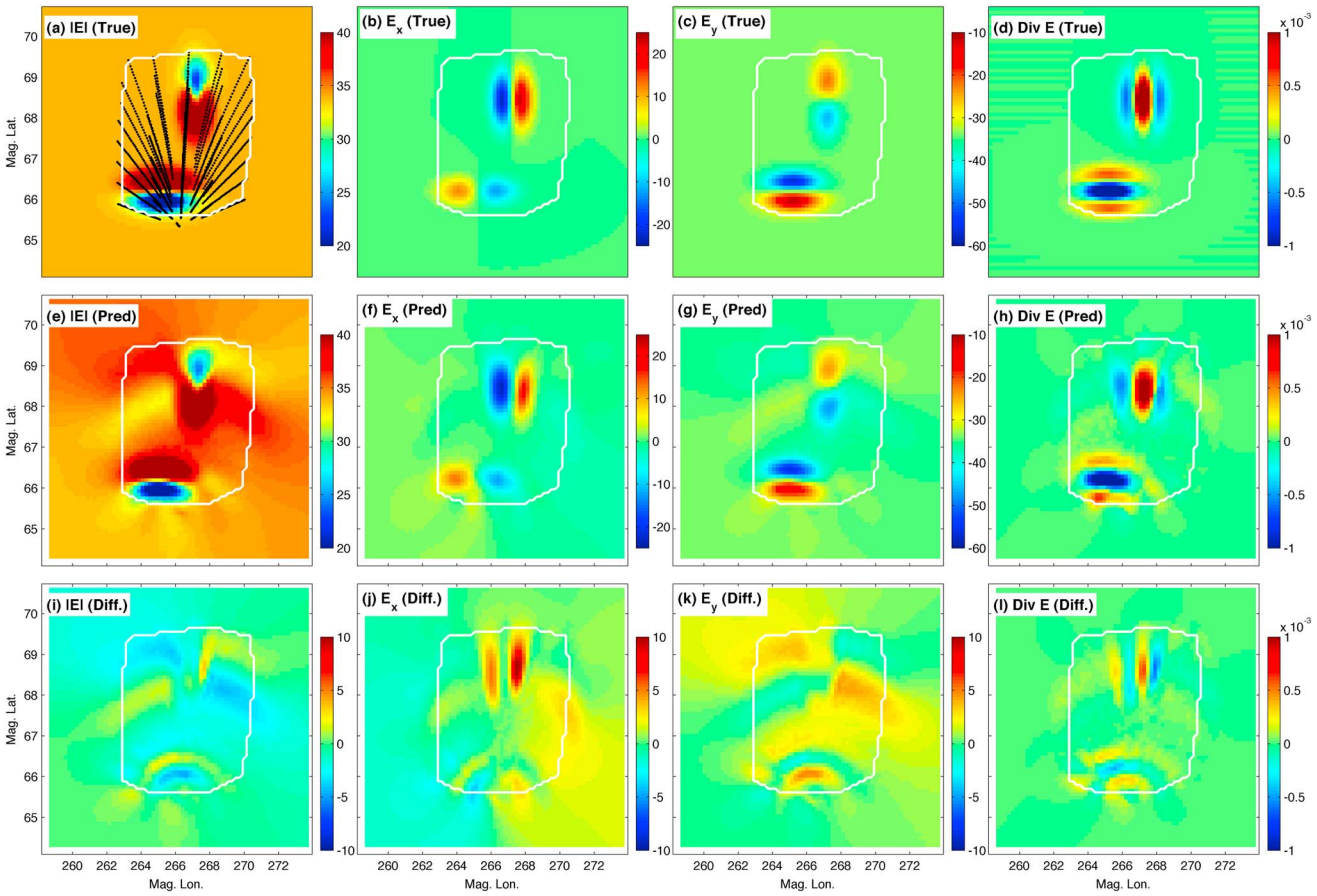

Figure 4. Same as Figure 1 for a two-blob case.

3. Toward the edges of the measured region, there is a transition between the part of the image that is well supported by the measurements and that where the regularization is dominant. This results in the appearance of curved features in the residuals and overall degraded performance with respect to the true image.
4. The fact that the reconstruction produces finite-sized blobs means that artificial E_x will appear to enforce the curl-free condition. These artifacts are seen toward the edges of the imaged region. However, they are small as compared to the overall magnitude of the electric field structure (note the different color scales on the E_x and E_y panels).
5. The main features of the electric field divergence are captured well; that is, a positive divergence peaked where the meridional electric field perturbation crosses zero and a negative divergence on either side. The magnitude of the electric field structure is also represented well.

To investigate the LOS velocity reconstructions, in Figure 2 we show the LOS-equivalent electric field and its reconstruction, concatenated for all beams. Figure 2 (top) shows the total LOS measurements, whereas Figure 2 (bottom) shows the LOS measurements after the background field estimate has been removed (i.e., these are the measurements that are used in the two-dimensional inversions). The final reconstruction (red) is in excellent agreement with the measurements (blue), which are in turn very close to the true values (black) for these small error levels. The background field shown in green captures the largest-scale variation. After removal of the background field, the residuals shown in the Figure 2 (bottom) illustrate the robust reproduction of the measurements using the two-dimensional algorithm.

In Figure 3 we show an example of a meridionally extended potential blob (combined with a constant background E_y field), again with small measurement errors, in the same form as Figure 1. The blob results in an meridionally extended structure in E_x which has a zero crossing in the zonal direction. Because of the

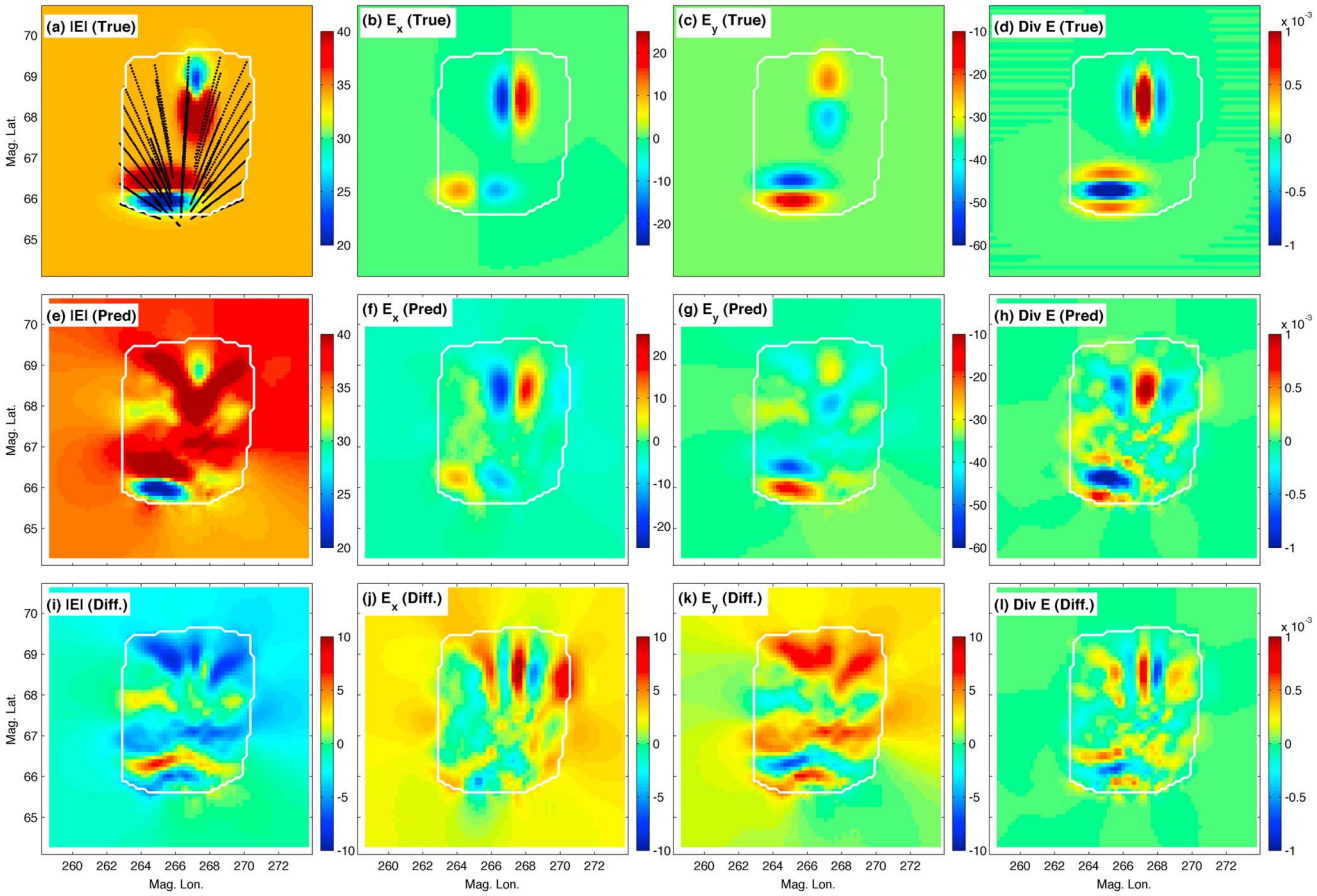

Figure 5. Same as Figure 4 with realistic measurement errors.

geometry of this problem, the flow velocity structures are mostly aligned with the orientation of the beams. As a result of this alignment, there are significant residuals after subtracting the background field as compared to the errors, which allow for robust reconstruction of the fields. Indeed, as shown in Figure 3, the reconstructions capture the main features of the fields and of the divergence, with some minor artifacts in E_y associated with the finite size of the reconstructed blobs.

As a more complicated example, Figures 4 shows a case with two small potential blobs, again sampled with small measurement errors. For this idealized case, the reconstructions are once again quite robust, with, in general, excellent reproductions in the main features of the electric field, its divergence, and its magnitude. For the same potential pattern, Figure 5 shows reconstructions with more realistic errors on the radar measurements (factor of 10 larger than in the previous cases), which are representative of typical ISR applications. A smooth reconstruction is produced that captures the essence of the electric field structures, while underestimating their magnitude. While this is only a single realization of the measured fields, the results are similar to the smaller error case with the main differences being (a) that some small artifacts have appeared in the reconstructions, most visible in the residuals, and (b) that the reconstructed features are smaller in magnitude. The artifacts are due to the particular realization of noise and thus we would expect that these features would be somewhat random in nature. The depressed magnitude is most visible in the E_y field of the higher latitude blob, a result of (a) the radar being least sensitive to the $\hat{y}$ component of the electric field and (b) the errors increasing with distance from the radar. "Muted" features are a general feature of our simulations with realistic measurement errors. They are the result of the fact that more emphasis will be placed on the a priori information in these cases, which minimizes curvature. Because our algorithm enforces a constraint on the total error rather than on the error for any single measurement, it is perfectly allowable that as the errors get larger, the algorithm might choose a solution that deviates from any given measurement by a value larger than what one might expect due to its individual error. The LOS measurements for the two cases

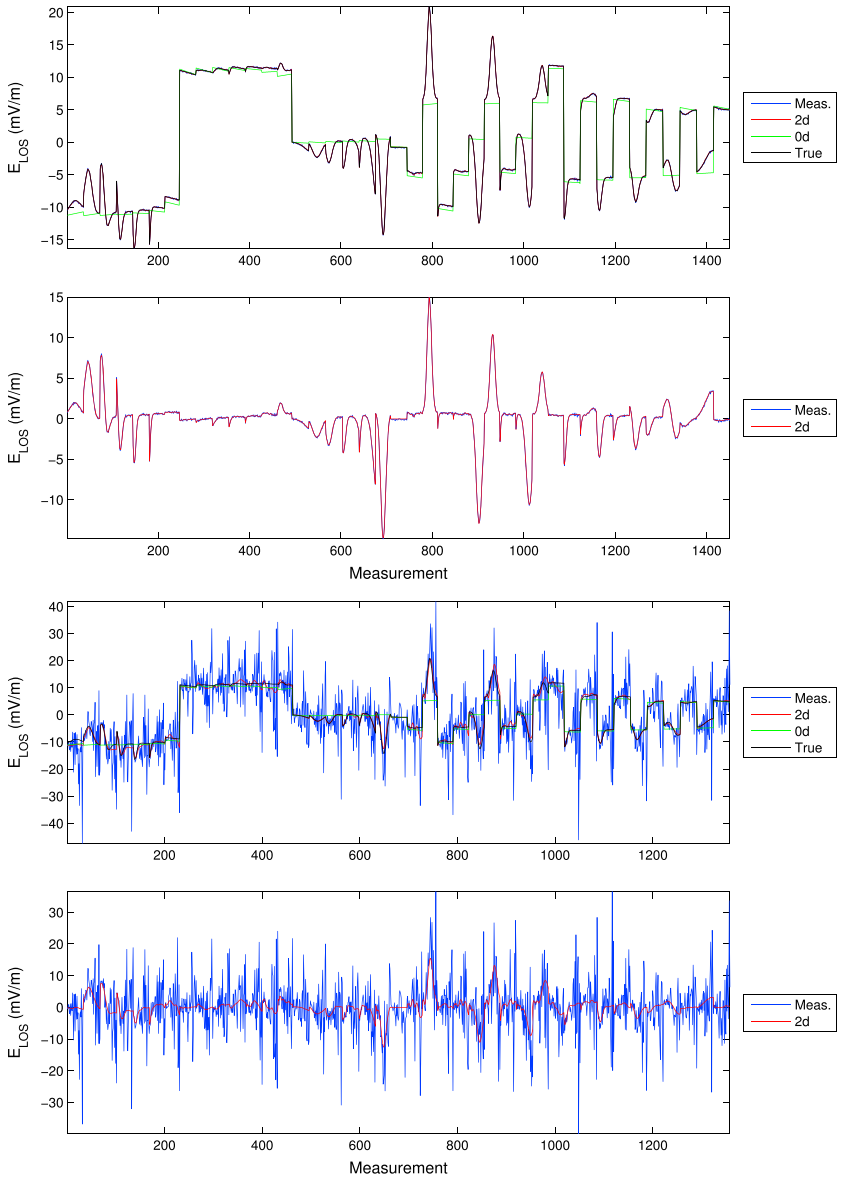

Figure 6. LOS measurements in the same form as Figure 2 for (top) small measurement errors and (bottom) realistic measurement errors.

are shown in Figure 6. In the realistic error case, it is quite impressive that the algorithm is able to reproduce features which are not that visible to the human eye with the significant uncertainties.

As discussed in section 2.4, the algorithm presented here also allows for an estimate of the a posteriori covariance matrix of the potential function, which can be propagated to estimate errors on the electric field. Errors on E_x and E_y are shown for the simulations with small and realistic measurement errors in Figure 7. The errors are smallest in the region of measurement and increase outside of that region. Outside of that region, they are completely determined by **G** as shown in equation (19). Because of this, we should not expect errors in this region to have any practical meaning, as we do not expect our a priori information to be valid in that region. In practice, we would simply not use imaging results outside of the measurement region. Inside the measurement region, the errors will be determined by both $\mathbf{G}^{-1}/\alpha$ (the a priori covariance matrix) and **C** (the measurement covariance matrix) with the relative contribution depending on the level of errors and the value of α. That is, if a very smooth solution is chosen, α will be large, and the error will be dominated by the measurement error. In the example shown, the output errors have increased by a factor of ~10, indicating that a large enough α has been found (smooth enough solution) for the errors to be dominated by

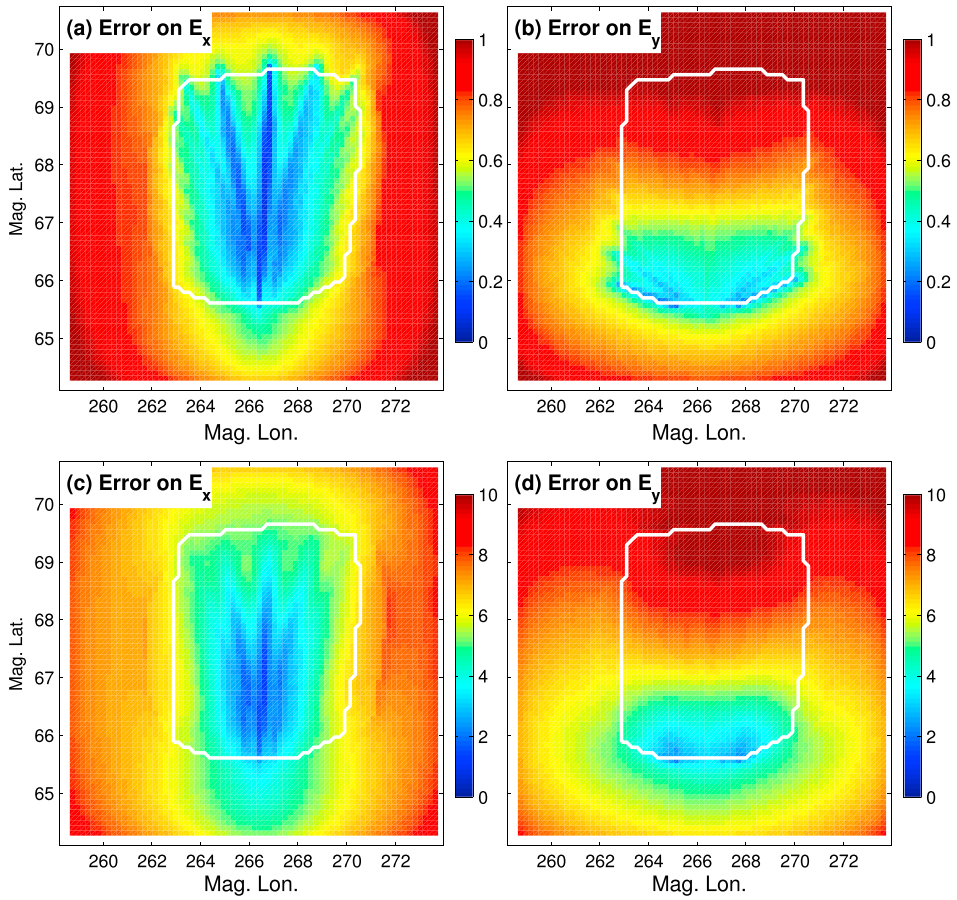

Figure 7. (a–d) Errors on the estimates for the small error case of Figures 4a and 4b and the larger error case of Figures 5c and 5d. Note that the color scale changes by an order of magnitude from the two examples.

the measurement errors. Most of the artifacts in the images (see Figure 5) are smaller than the errors on the fields. The errors on E_x show structuring that mimic the sampling of the beams, a result of the fact that the beams are nearly aligned with the direction of the $\mathbf{E} \times \mathbf{B}$ flow leading to good estimates of that component of the electric field where the field is sampled. E_y, on the other hand, shows errors that increase with latitude presumably due mainly to the errors increasing with range squared.

We have presented results for extended blobs and localized blobs. Localized features confined to the field of view are more easily reproducible by the algorithm. In general, long-wavelength structures as compared to the measurement region will be poorly reproduced. As discussed earlier, this makes challenging the case of simple gradients, for which other approaches such as boundary specification using other data sources may be necessary. Finally, a general feature of the simulations is that the magnitude and divergence are fairly well produced, perhaps better than the fields themselves. The algorithm appears to be surprisingly good at estimating electric field divergence, which is somewhat surprising given that those quantities depend on derivatives.

3.2. Examples With Real Data

Figure 8 shows two examples of imaging results for E_x and E_y from PFISR using the same 41-beam imaging mode used in section 3.1. From equation (24), the existence and uniqueness of the solution does not depend on the number of beams (as long as $N \gg 1$), and the choice of beam configuration constitutes a trade-off between temporal and spatial resolutions. In making this choice it should be considered that the imaging algorithm balances the information in nearby data points so that temporal resolution may not be much degraded by replacing a single beam with two, even though each has half the averaging period of the single beam. However, because the ISR spectral fitting process used to extract the LOS velocities is

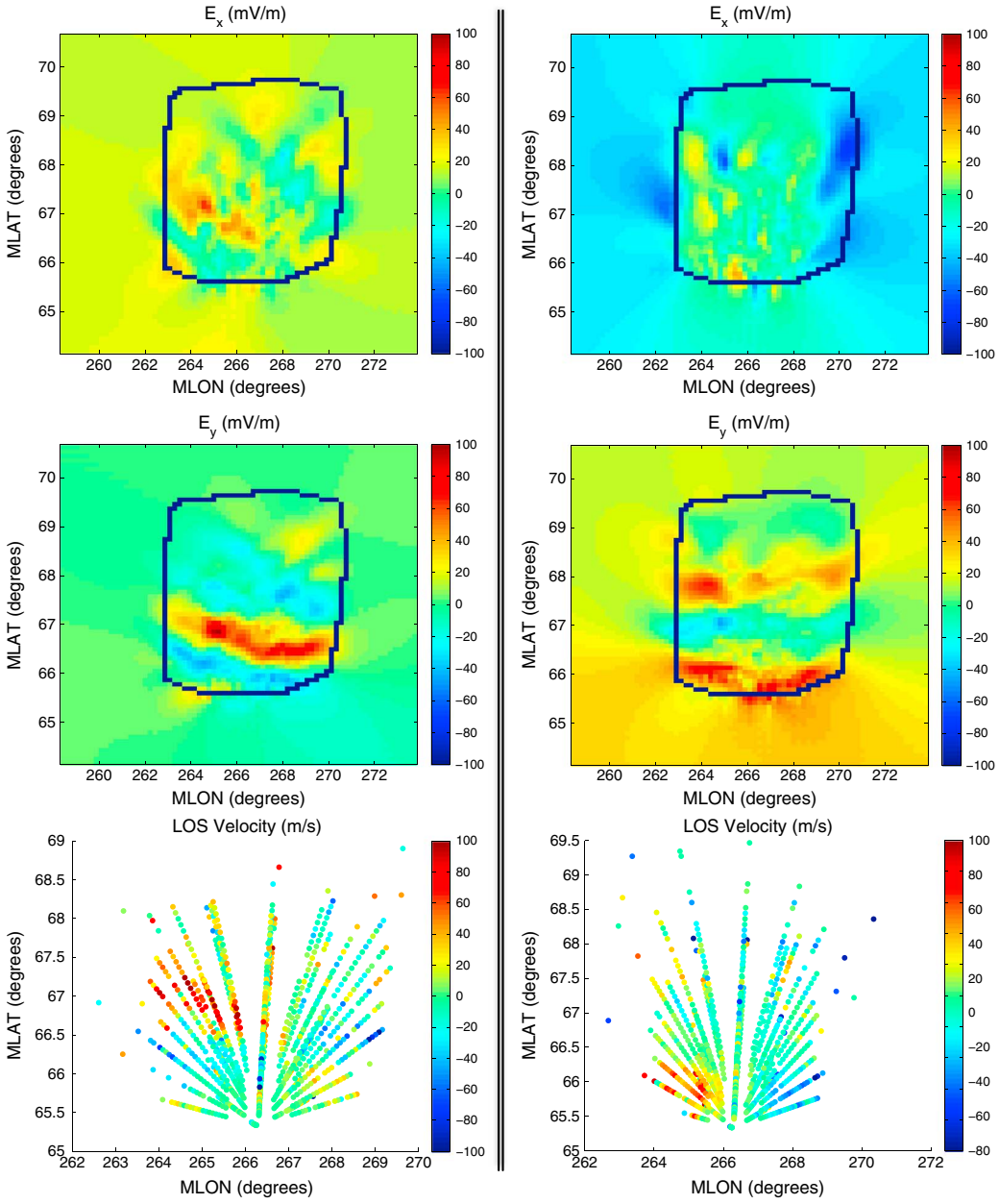

Figure 8. Two examples of comparisons of PFISR LOS velocity with the produced image. (top row) E_x, (middle row) E_y, and (bottom row) the LOS velocity for each beam and range gate, as a function of magnetic latitude and longitude. The jagged blue enclosures delineate the regions with measurement support, where the curvature is used for regularization. Outside the enclosures the gradient is used for regularization so that the solution approaches a constant far from the measurements.

nonlinear, the effect of increasing the number of beams cannot be evaluated using linear methods. At present, the choice of 41 beams is one of judgement, for the purposes of example.

The two examples are shown in the left and right columns of Figure 8. Figure 8 (bottom row) shows scatterplots of the LOS velocities measured by the individual beams. Flow across the radar's boresight manifests as negation of the LOS velocity across the boresight, which is evident in some areas. These areas correspond to an electric field along the boresight, which is aligned with the magnetic meridian ($\hat{y}$). The E_y components are shown in Figure 8 (middle row). An LOS velocity signature that does not reverse across the boresight is associated with flow along the boresight and indicates an electric field in the zonal direction ($\hat{x}$). A zonal

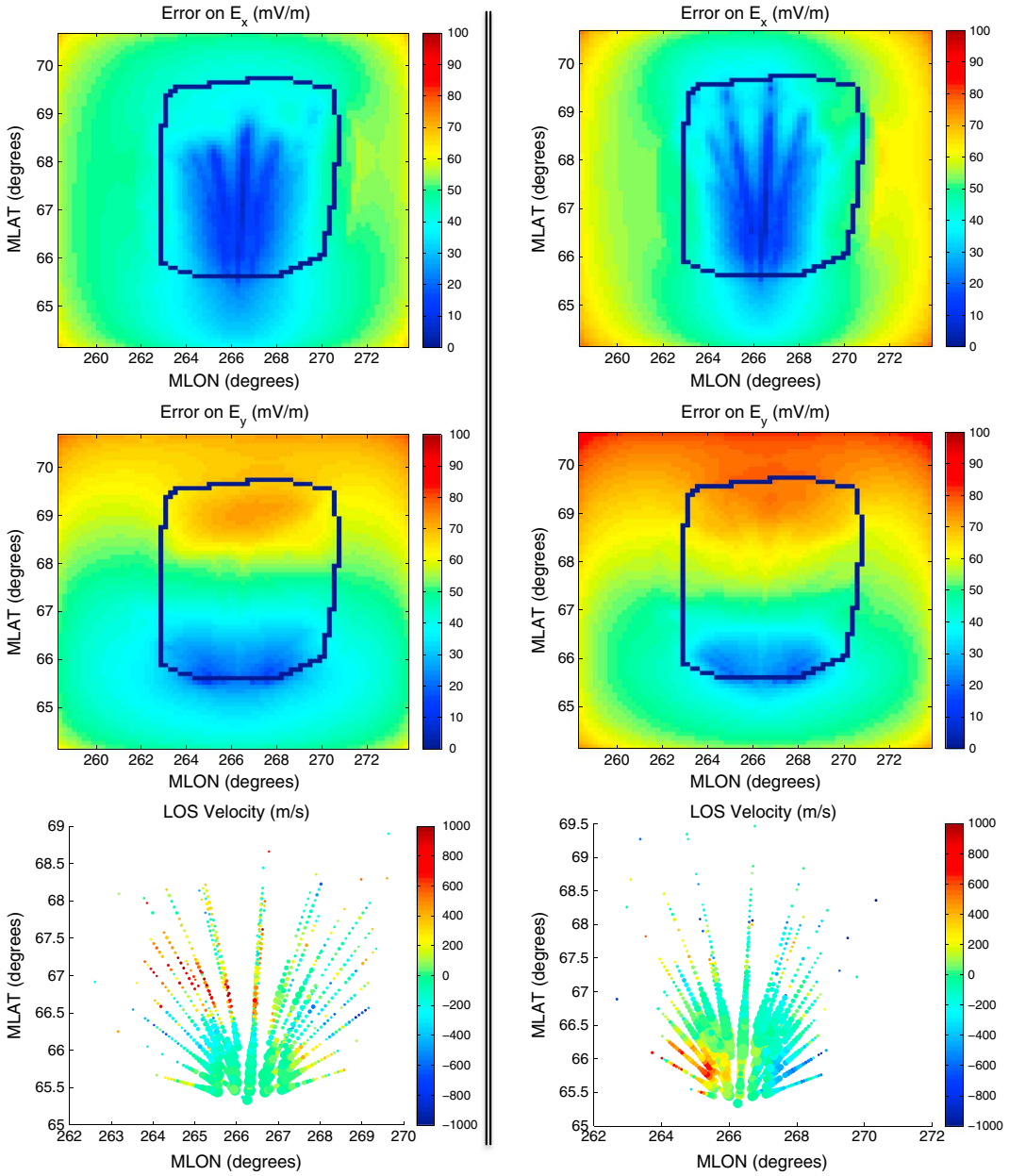

Figure 9. Two examples of comparisons of PFISR LOS velocity error and beam pattern with the error estimate produced for the image. (top row) Error on E_x, (middle row) error on E_y, and (bottom) the LOS velocities for each beam and range gate, as a function of magnetic latitude and longitude, where the marker size is inversely proportional to the measurement error. The jagged blue enclosures delineate the regions with measurement support, where the curvature is used for regularization. Outside the enclosures the gradient is used for regularization.

electric field is less common in nature and is not very evident in these examples. The E_x components are shown in Figure 8 (top row).

The imaging algorithm is tasked with assembling the LOS velocity information in the distributed beams in order to determine the direction of flow at each point in the image and hence distinguish between E_x and E_y. Through the minimum curvature criteria, the algorithm emphasizes data points with a consistent spatial distribution and, to the extent that the measurements have error, deemphasizes disparate points. Examination of Figure 8 shows the algorithm at work on real measurements. Regions of localized auroral arc-like fields (enhanced E_y) are observed in both examples, and indeed, these correlate well with optical images (not shown, and will be explored in future studies).

Figure 9 shows the error estimated for the images in Figure 8. In Figure 9, the marker size for the LOS velocities (bottom row) is inversely proportional to the measurements error. Examining the figure, it can be seen how the reconstruction error depends on both the measurement error for the individual LOS velocities and also on the spatial distribution of the measurements. The example on the right exhibits smaller error in E_x in the high-latitude portion, apparently due to smaller measurement errors on the three central beams, which are nearly aligned with the $\mathbf{E} \times \mathbf{B}$ flow from E_x. On the other hand, the example on the left exhibits smaller error in E_y in the high-latitude portion, apparently due to better zonal filling of the LOS samples, which give information on flow across the radar's boresight.

4. Discussion and Conclusion

An algorithm has been developed to estimate the two-dimensional electric field distribution from the LOS velocity measurements made by multibeam ISRs and to assign error estimates to the pixels of this electric field "image." The electric field distribution is underdetermined by the LOS velocities, and determining the image is a problem in regularization, that is, in selecting a reasonable solution from the family of solutions that match the data within the measurement error. We use the method of Lagrange multipliers to identify the solution that minimizes a measure of curvature and gradient from the set of solutions that realize the most probable value for the χ^2 statistic. The measure emphasizes curvature where there is good support from the measurements and emphasizes gradient outside of this region in order to effect a relatively uniform approach to an unspecified boundary. The error in the reconstructed image is estimated by mapping the mathematical form to a Bayesian estimate, and observing that the Lagrangian method uses the measure of curvature and gradient to establish an effective a priori covariance matrix. The condition for existence and uniqueness of the solution is that on average, the errors in the LOS velocities should be smaller than the LOS velocities (equation (24)).

Examples of the algorithm applied to synthetic data are presented in section 3.1. Simulations of large-scale electric potential blobs extended zonally (Figure 1) and meridionally (Figure 3) result in blobs localized within the region well supported by the measurements, with the fields going to constant values outside of this region. This is the best that we can expect the algorithm to perform without additional information on the scale size of the structures. However, as expected, the estimated errors become large outside of the measurement region. Simulations of localized blobs with idealized and realistic measurement errors demonstrate that complex features can be reproduced by the algorithm. The main consequences of added measurement noise are "noisier" images and muted features. The former effect can be evaluated by assessing the a posteriori covariance matrix, and the latter effect is a consequence of the minimum curvature with total error constraint approach that we have taken. This choice ensures that features must be well supported by the measurements to appear in the final images.

Thus, the main limitation of the approach is with respect to structures with scales larger than the region probed by the radar. This limitation is not related to the Lagrangian algorithm but is instead an inherent consequence of the monostatic radar geometry. For example, attempting to fit a constant gradient solution to the LOS data is unreliable and often results in an excessive gradient. This is a manifestation of the usual limitations in Fourier reconstruction with respect to the size of the region covered by the data sample. We must be content with reconstructing features that fit within the field of view of the experiment. In this regard, we might note that the Resolute Bay Incoherent Scatter Radar achieves a larger field of view for imaging because the steeper angle of the antenna face allows for beams that are more nearly horizontal.

Examples of the algorithm applied to real data from PFISR are presented in section 3.2. The images produced are compared with the LOS velocities measured along individual beams. Examining these results (Figure 8), it is seen how the algorithm interprets the spatial distribution of LOS velocities in a way consistent with human evaluation and possibly exceeding it; considering the number of factors that must be balanced, it would be difficult for a human to do as good a job in reconstructing E_x and E_y. The error estimated for the reconstructions is presented in Figure 9 and appears useful for evaluating the reliability of the images produced.

In future work, we plan to use the methodology to study current systems associated with auroral arcs. The simulations conducted have shown that the algorithm is robust in its representation of the magnitude and divergence of the electric field, which are important for evaluating current systems and Joule heating rates. It is somewhat surprising that the algorithm is good at estimating divergence, since this quantity depends

on derivatives and is not normally addressed by ISR measurements at all. We have also developed a methodology for three-dimensional imaging of the electron density (not shown). Assuming that the electric field maps along the geomagnetic field, and using model results for collision frequency, the images of electron density allow derivation of three-dimensional current. For example, we hope to be able to distinguish Type I and Type II arcs [*Bostrom*, 1964; *Haerendel*, 2011] and thereby make inferences as to physical source.

Acknowledgments
This work was supported by National Science Foundation (NSF) grants AGS-1242913, AGS-1133009, and AGS-1344300. The Poker Flat Incoherent Scatter Radar is operated by SRI International on behalf of the U.S. National Science Foundation under NSF Cooperative Agreement AGS-1133009. PFISR data used in this paper are available from http://amisr.com or by contacting the authors.

References

Bostrom, R. (1964), A model of the auroral electrojets, *J. Geophys. Res.*, *69*(23), 4983–4999.
Boyd, S., and L. Vandenberghe (2009), *Convex Optimization*, Cambridge Univ. Press, Cambridge, U. K.
Butler, T. W., J. Semeter, C. J. Heinselman, and M. J. Nicolls (2010), Imaging F region drifts using monostatic phased array incoherent scatter radar, *Radio Sci.*, *45*, RS5013, doi:10.1029/2010RS004364.
Cosgrove, R. B., et al. (2013), Empirical model of Poynting flux derived from FAST data and a cusp signature, *J. Geophys. Res. Space Physics*, *118*, 411–430, doi:10.1002/2013JA019105.
Dahlgren, H., J. L. Semeter, K. Hosokawa, M. J. Nicolls, W. Butler, M. G. Johnsen, K. Shiokawa, and C. Heinselman (2012), Direct three-dimensional imaging of polar ionospheric structures with the Resolute Bay Incoherent Scatter Radar, *Geophys. Res. Lett.*, *39*, L05104, doi:10.1029/2012GL050895.
Dougherty, J. P., and D. T. Farley (1960), A theory of incoherent scattering of radio waves by a plasma, *Proc. R. Soc. London A*, *259*, 79–99.
Goldstein, H. (1980), *Classical Mechanics*, Addison-Wesley, Reading, Mass.
Haerendel, G. (2011), Six auroral generators: A review, *J. Geophys. Res.*, *116*, A00K05, doi:10.1029/2010JA016425.
Heinselman, C. J., and M. J. Nicolls (2008), A Bayesian approach to electric field and E-region neutral wind estimation with the Poker Flat Advanced Modular Incoherent Scatter Radar, *Radio Sci.*, *43*, RS5013, doi:10.1029/2007RS003805.
Hysell, D. L., and J. L. Chau (2006), Optimal aperture synthesis radar imaging, *RS2003*, *41*, doi:10.1029/2005RS003383.
Kelly, J. D., C. J. Heinselman, J. F. Vickrey, and R. R. Vondrak (2009), Initial results from Poker Flat Incoherent Scatter Radar (PFISR), *J. Atmos. Sol. Terr. Phys.*, *71*, 635, doi:10.1016/j.jastp.2009.01.009.
Neumaier, A. (1998), Solving ill-conditioned and singular linear systems: A tutorial on regularization, *SIAM Rev.*, *40*, 636–666.
Nicolls, M. J., C. J. Heinselman, E. A. Hope, S. Ranjan, M. C. Kelley, and J. D. Kelly (2007), Imaging of Polar Mesosphere Summer Echoes with the 450 MHz Poker Flat Advanced Modular Incoherent Scatter Radar, *Geophys. Res. Lett.*, *34*, L20102, doi:10.1029/2007GL031476.
Nygren, T., A. T. Aikio, R. Kuula, and M. Voiculescu (2011), Electric fields and neutral winds from monostatic incoherent scatter measurements by means of stochastic inversion, *J. Geophys. Res.*, *116*, A05305, doi:10.1029/2010JA016347.
Semeter, J., T. Butler, C. Heinselman, M. Nicolls, J. Kelly, and D. Hampton (2009), Volumetric imaging of the auroral ionosphere: Initial results from PFISR, *J. Atmos. Sol. Terr. Phys.*, *71*, 738–743, doi:10.1016/j.jastp.2008.08.014.
Semeter, J., T. W. Butler, M. Zettergren, C. J. Heinselman, and M. J. Nicolls (2010), Composite imaging of auroral forms and convective flows during a substorm cycle, *J. Geophys. Res.*, *115*, A08308, doi:10.1029/2009JA014931.
Skolnik, M. (1980), *Introduction to Radar Systems*, McGraw-Hill, New York.